Three-dimensional instabilities in a discretely heated annular flow: Onset of spatio-temporal complexity via defect dynamics

Juan M. Lopez and Francisco Marques

Articles you may be interested in

Spatio-temporal and modal analysis of unsteady fluctuations in a high-subsonic base flow
Phys. Fluids **26**, 086101 (2014); 10.1063/1.4891257

Three-dimensional swirling flows in a tall cylinder driven by a rotating endwall
Phys. Fluids **24**, 014101 (2012); 10.1063/1.3673608

Revisiting the two first instabilities of the flow in an annular rotor-stator cavity
Phys. Fluids **21**, 064106 (2009); 10.1063/1.3156859

Stability analysis of natural convective flows in horizontal annuli: Effects of the axial and radial aspect ratios
Phys. Fluids **18**, 104107 (2006); 10.1063/1.2364027

Amplification of boundary layer instability by hot wall thermal oscillation in a side heated cavity
Phys. Fluids **17**, 014103 (2005); 10.1063/1.1828122

Three-dimensional instabilities in a discretely heated annular flow: Onset of spatio-temporal complexity via defect dynamics

Juan M. Lopez[1,a)] and Francisco Marques[2]

[1]*School of Mathematical and Statistical Sciences, Arizona State University, Tempe, Arizona 85287, USA*
[2]*Department of Físca Aplicada, Universitat Politècnica de Catalanya, Girona s/n, Mòdul B4 Campus Nord, 08034 Barcelona, Spain*

The transition to three-dimensional and unsteady flow in an annulus with a discrete heat source on the inner cylinder is studied numerically. For large applied heat flux through the heater (large Grashof number Gr), there is a strong wall plume originating at the heater that reaches the top and forms a large scale axisymmetric wavy structure along the top. For $Gr \approx 6 \times 10^9$, this wavy structure becomes unstable to three-dimensional instabilities with high azimuthal wavenumbers $m \sim 30$, influenced by mode competition within an Eckhaus band of wavenumbers. Coexisting with some of these steady three-dimensional states, solution branches with localized defects break parity and result in spatio-temporal dynamics. We have identified two such time dependent states. One is a limit cycle that while breaking spatial parity, retains spatio-temporal parity. The other branch corresponds to quasi-periodic states that have globally broken parity. © *2014 AIP Publishing LLC*.
[http://dx.doi.org/10.1063/1.4881435]

I. INTRODUCTION

Interest in natural convection in enclosures has a long history,[1] motivated by both relevance in many practical situations as well as being a fundamental problem. The early studies[2–4] focused on two-dimensional rectangular enclosures with isothermal vertical walls maintained at different constant temperatures, and the top and bottom walls were typically modeled as being insulating. For sufficiently large temperature differences across the vertical walls, convective flow is restricted to thin boundary layers on each wall and the core region in between the vertical boundary layers has a stable vertical temperature gradient with essentially no vertical flow.

From a practical perspective, vertical walls with prescribed heat flux, rather than prescribed temperature, are very much of interest. However, these have received considerably less attention, in part due to the longer transients associated with the isoflux (Neumann) boundary conditions compared to the isothermal (Dirichlet) boundary conditions.[5] In one of the earliest studies to consider natural convection in a cavity with uniform heat fluxes imposed on the vertical walls, Kimura and Bejan[6] determined the boundary layer structure on the vertical walls and showed that the flow in the core between the walls is essentially linearly stably stratified in temperature with virtually no flow; all the flow is confined to the boundary layers, whose thickness is constant, much as was found for the constant temperature vertical walls.[4] Scaling laws for the Prandtl number dependence of the boundary layer on a vertical plate heated with uniform heat flux in an initially linearly stratified ambient fluid have recently been developed.[7] All of these studies with isoflux conditions were restricted to planar two-dimensional flows.

a)Electronic mail: jmlopez@asu.edu

    26, 064102-1

It is only quite recently that three-dimensional numerical studies of natural convection between two vertical walls maintained at fixed different temperatures have been presented, and for the most part they have treated the vertical and horizontal spanwise directions as being periodic (thus neglecting endwall effects).[8–10] The primary instability of such a system has been shown to be two-dimensional, invariant in the spanwise and periodic in the vertical direction, and three-dimensional flow structures result as secondary instabilities. All of these instabilities are in the bulk and not boundary layer instabilities.

On the other hand, there have been extensive studies of two-dimensional natural convection in enclosures at large Rayleigh or Grashof numbers where the thin vertical wall boundary layer flows become wavy as they are turned at the ceiling (and/or the floor), at least transiently, and the waves are of large enough amplitude to cause separation and locally reversed flow. These ceiling jets and trailing waves and recirculation zones have been observed experimentally,[11–14] in differentially heated rectangular cavities with zero-flux top and bottom walls, but their analysis in terms of boundary layer analysis and numerical simulation have been restricted to two-dimensional planar flows.[15–18]

In many practical applications, some of the walls are only partially heated, e.g., electronic components are often modeled as having discrete heat sources. The question then arises as to what extent does the dynamics associated with the often-studied uniformly heated slots apply to finite enclosures with discrete heater elements. To allow for a three-dimensional geometry, but retaining a two-dimensional basic flow state, natural convection in an annulus has often been studied.[19,20] In a recent study,[21] the characteristics of the basic state (BS) for natural convection in a unit aspect ratio annulus driven by a constant heat-flux finite segment on the inner cylinder were determined numerically. For low applied heat flux through the heater, as measured non-dimensionally by a Grashof number, Gr, the flow in the annular gap consists of a weak single-cell overturning meridional flow driven by the radial temperature gradient between the heater on the inner cylinder and the cold outer cylinder and heat is transported primarily via conduction. For $Gr > 10^5$, the nonlinear convection terms become more important, heat transfer is convection-dominated and the flow becomes segregated into three distinct regions, with the flow dominated by thin boundary layers and a ceiling jet on the upper endwall. The axisymmetric computed flows remained steady up to $Gr \sim 10^{10}$, but stability to three-dimensional perturbations was not determined. This is the subject of the present paper.

II. GOVERNING EQUATIONS

A schematic of the flow is given in Fig. 1, showing an annulus of height H, inner radius R_i, and outer radius R_o. The top and the bottom endwalls are thermally insulated and the outer cylinder is maintained at a fixed cold temperature Θ_0. A heater element on the inner cylinder provides a
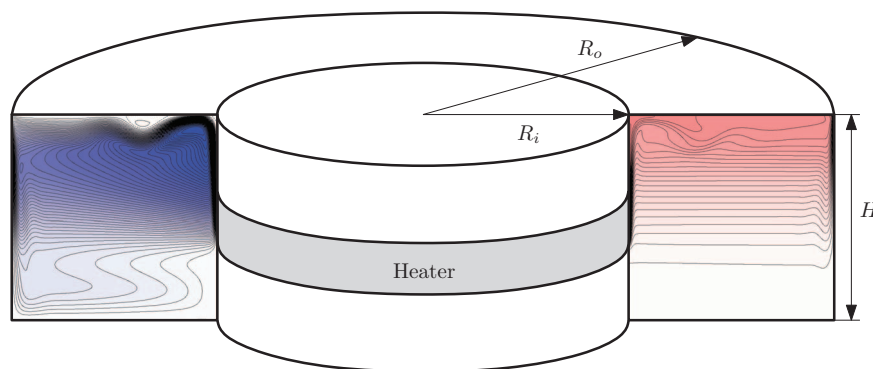

FIG. 1. Flow schematic showing streamlines, ψ, on the left and isotherms, T, on the right of the steady axisymmetric basic state at $Gr = 5 \times 10^9$. There are 50 positive (red) and 50 negative (blue) contours in the ranges $T \in [0, 0.015]$ and $\psi \in [-55, 55]$.

constant heat flux Q, and the rest of the inner cylinder is insulated. The fluid of kinematic viscosity ν in the annulus is Newtonian and the Boussinesq approximation is employed with gravity, g, pointing in the negative axial direction.

The annular gap, $(R_o - R_i)$, is used as the length scale, the thermal diffusion time across the gap, $(R_o - R_i)^2/\kappa$, is the time scale, and the temperature scale is $Q(R_o - R_i)/k$, where κ is the thermal diffusivity and k is the thermal conductivity of the fluid. The non-dimensional temperature relative to the temperature of the outer cylinder is $T = (\Theta - \Theta_0)k/Q(R_o - R_i)$. The flow is governed by the Grashof number, $Gr = g\beta Q(R_o - R_i)^4/k\nu^2$, and the Prandtl number, $\sigma = \nu/\kappa$. Geometric parameters describing the aspect and radius ratios of the annulus, as well as the heater location and length, have quantitative effects, but not qualitative effects over a considerable range of values.[21]

The non-dimensional governing equations are

$$(\partial_t + \boldsymbol{u} \cdot \nabla)\boldsymbol{u} = -\nabla p + \sigma \nabla^2 \boldsymbol{u} + GrT\hat{\boldsymbol{z}}, \tag{1}$$

$$(\partial_t + \boldsymbol{u} \cdot \nabla)T = \nabla^2 T, \quad \nabla \cdot \boldsymbol{u} = 0, \tag{2}$$

where $\boldsymbol{u}$ is the velocity field, p is the dynamic pressure, and $\hat{\boldsymbol{z}}$ the unit vector in the vertical direction z.

The boundary conditions are no-slip and as all boundaries are stationary the velocity is zero on all boundaries. For the temperature, it is held constant $T = 0$ on the outer cylinder, $r = r_o$. The top and bottom, $z = \pm 0.5$, have zero heat flux so $\partial T/\partial z = 0$. On the inner cylinder $r = r_i$, $\partial T/\partial r = -1$ at the heater, and $\partial T/\partial r = 0$ elsewhere. This idealized step-function profile for the heat flux at the inner cylinder is on the one hand never exactly realized in a physical experiment, and on the other hand causes numerical problems (Gibbs phenomenon) when a spectral discretization is used. As such, we shall use a smoothed version corresponding to

$$\partial T/\partial r = -0.5\left[\tanh(\alpha(z - z_1)) + \tanh(\alpha(z_2 - z))\right]. \tag{3}$$

In the present study, we use $\alpha = 100$ which determines the distance over which the steps are smoothed, and $z_1 = -z_2 = 0.125$, which corresponds to placing a heater over one quarter of the inner cylinder symmetrically about the mid-height $z = 0$. Also for the present study, we shall fix the aspect ratio $\Gamma = H/(R_o - R_i) = 1$, the radius ratio $R_i/R_o = 0.5$, and the Prandtl number $\sigma = 1$, and consider the response to variations in the Grashof number Gr.

The governing equations are solved using a second-order time-splitting method with consistent boundary conditions for the pressure.[22,23] Spatial discretization is via a Galerkin-Fourier expansion in θ and Chebyshev collocation in r and z. To solve this problem, the hydrodynamic code of Ref. 24 was extended to solve the temperature equation. The resolution used throughout this paper is $n_r \times n_z \times n_\theta = 150 \times 150 \times 256$ and $\delta t = 2 \times 10^{-7}$, although resolution tests were conducted on some cases using $n_\theta = 512$.

The governing equations and boundary conditions are invariant under arbitrary rotations about the axis, R_α, and reflections through meridional planes, K_β. The actions of these symmetries on the velocity and temperature are

$$R_\alpha(u, v, w, T)(r, \theta, z, t) = (u, v, w, T)(r, \theta + \alpha, z, t); \quad \alpha \in [0, 2\pi), \tag{4}$$

$$K_\beta(u, v, w, T)(r, \theta, z, t) = (u, -v, w, T)(r, 2\beta - \theta, z, t); \quad \beta \in [0, 2\pi). \tag{5}$$

R_α and K_β do not commute: $K_\beta R_\alpha = R_{-\alpha} K_\beta$, and together they generate the group $O(2)$ acting on the periodic θ-direction. The system is also invariant under time translations. As such, the basic state is steady, axisymmetric, and purely poloidal, i.e., it has zero azimuthal velocity and zero axial and radial vorticity

$$\boldsymbol{u}_b = (u, 0, w)(r, z) \quad \text{and} \quad \nabla \times \boldsymbol{u}_b = (0, \eta, 0)(r, z). \tag{6}$$

The bifurcations from the basic state to three-dimensional flows are conveniently diagnosed using the modal kinetic energies

$$E_m = \int_0^{2\pi} \int_{-\Gamma/2}^{\Gamma/2} \int_{r_i}^{r_o} \boldsymbol{u}_m \boldsymbol{u}^*_m r \mathrm{d}r \mathrm{d}z \mathrm{d}\theta \,, \qquad (7)$$

where $\boldsymbol{u}_m$ is the mth azimuthal Fourier mode of the velocity field and $\boldsymbol{u}^*_m$ is its complex conjugate.

III. BASIC STATE AND ITS AXISYMMETRIC INSTABILITY AT LARGE *Gr*

A typical basic state at large Gr number is presented in Fig. 1, which shows isotherms and streamlines in a meridional plane of the steady, axisymmetric basic state at $Gr = 5 \times 10^9$. Below the level of the bottom of the heater, an essentially cold stagnant pool develops, and the heat flux through the outer cylinder in this region is essentially zero. Between the bottom and the top of the heater, most of the region in between the two cylinders is stably stratified with a relatively weak radial flow from the cold outer to the heated inner cylinder. The horizontal isotherms adjust to the temperatures on the cylinders in thin buoyancy boundary layers which drive fluid down the cold cylinder and up the heated cylinder segment. Above the heater top, the boundary layer flow from the heater continues upward where it meets the top endwall and turns into a ceiling jet that becomes wavy. Flow separation on the top wall leads to the formation of a recirculation zone there. The vast majority of the heat flux through the outer cylinder occurs at this upper level, and is heavily concentrated near the very top.

With the equations restricted to being axisymmetric, i.e., restricted to the $O(2)$ symmetric subspace, we have found that the basic state loses stability via a supercritical Hopf bifurcation at about $Gr = 7 \times 10^{10}$, resulting in a time-periodic flow corresponding to an oscillation of the large wave in the upper annulus above the heater section. However, the basic state becomes unstable to non-axisymmetric perturbations at considerably smaller Gr.

IV. THREE-DIMENSIONAL INSTABILITIES

Considering the full three-dimensional governing equations, the basic state first becomes unstable to three-dimensional perturbations at $Gr = Gr_{\text{crit}} \approx 5.9 \times 10^9$, which is an order of magnitude smaller than the critical Gr for the axisymmetric Hopf bifurcation.

Figure 2 summarizes the modal kinetic energies of the various states we have found. Part (a) of the figure gives the mean modal energy E_0. There are two main points to extract from this plot. First, there is a multiplicity of stable states co-existing for the same parameter values, and second, their
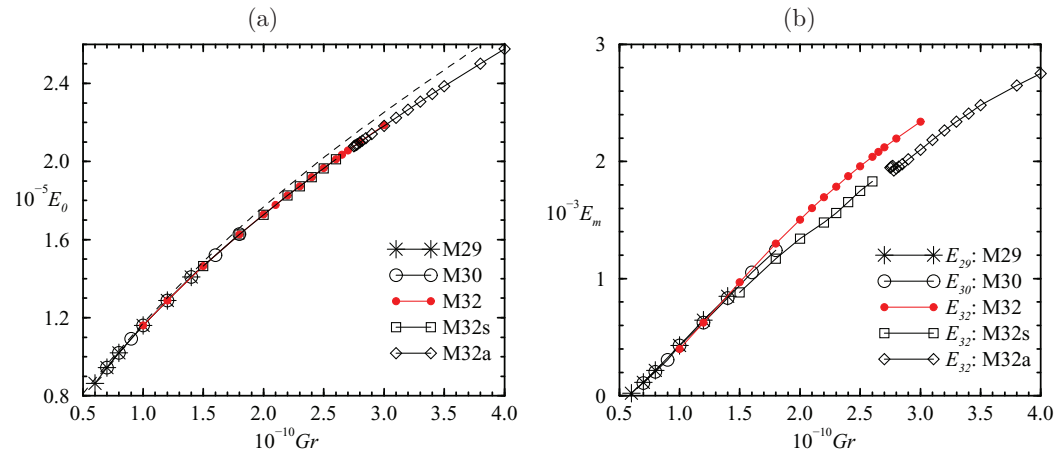

FIG. 2. Variations of (a) the mean modal energy E_0 and (b) the primary three-dimensional modal energies E_m versus Gr. The dashed line in part (a) is the E_0 of the underlying unstable steady axisymmetric state.

E_0 values differ by a very small amount (typically less than a few parts in 10^4). The dashed line in Fig. 2(a) is the E_0 of the underlying steady axisymmetric state which has lost stability (determined by computing in the axisymmetric subspace); the difference is zero at onset of instability and the mean E_0 of the three-dimensional state is progressively smaller than that of the axisymmetric state, but the difference remains small (less than about 2%) over the range of Gr considered. Part (b) of the figure gives the modal kinetic energy in the principal azimuthal wavenumber of the state. Here, there is a more discernible difference between the different flow states. There are three steady states, M29, M30, and M32 which are described first below, and two time-dependent families of states M32s and M32a which we describe later.

A. Three-dimensional steady states

As Gr is increased beyond 5.88×10^9, the basic state loses stability to a non-axisymmetric solution with an azimuthal wavenumber $m = 29$ disturbance that is localized on the stationary ceiling wave. Figure 3(a) shows isosurfaces for $Gr = 6 \times 10^9$ of the azimuthal vorticity, η, showing that the ceiling wave that was axisymmetric at lower Gr, now has an azimuthal waviness. This waviness is of very low amplitude for Gr values very close to onset. In order to visualize the three-dimensional perturbation, Fig. 3(b) shows the three-dimensional contribution to η by subtracting the axisymmetric part of the flow, to give $\eta - \eta_0$. The $m = 29$ perturbation consists of 29 pairs of counter rotating vortices. The size of these vortices is comparable to the thickness of the velocity boundary layer before it reaches the top lid, suggesting that the viscous boundary layer is involved in the selection of m. The signatures of these vortices on the top endwall are shown in part (c) of the figure and the corresponding thermal signature, $T - T_0$, is plotted in part (d). These vortex pairs are
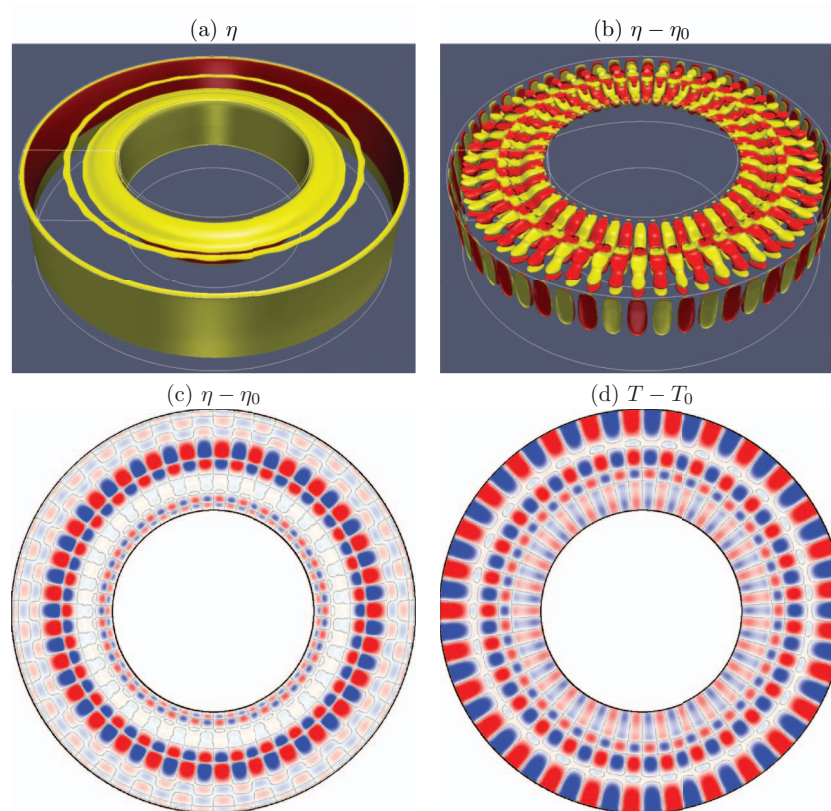

(a) η	(b) $\eta - \eta_0$
(c) $\eta - \eta_0$	(d) $T - T_0$

FIG. 3. Isosurfaces of (a) the azimuthal vorticity, and (b) the three-dimensional contribution of M29 at $Gr = 6.0 \times 10^9$; the isosurfaces for η are $\pm 1.5 \times 10^4$, and for $\eta - \eta_0$ they are at ± 200. Contours of (c) $\eta - \eta_0$ at the top endwall (levels between ± 500) , and (d) $T - T_0$ (levels between $\pm 10^{-6}$).

very similar to Görtler vortices,[25, 26] and are due to the curvature of the wall jet as it is turned at the ceiling leading to centrifugal instability, and also, when the ceiling jet rebounds, a second layer of Görtler vortices is formed of the opposite sense due to the change in the sense of curvature.

The Görtler instability is a boundary layer instability that results from curvature in the streamwise direction. Pairs of counter-rotating vortices develop in the boundary layer whose spanwise wavelengths are of the order of the boundary layer thickness. Theoretical treatments of Görtler vortices are highly idealized, usually assuming that the radius of curvature is constant and that the flow is parallel in the streamwise direction. This has lead to theoretical results that are difficult to interpret physically, namely, that the idealized Görtler linear stability analysis predicts growth at zero spanwise wavenumber ($m = 0$). In the review article,[25] it is noted that disturbances play an important role in the instability and that the growth rate of the instability depends on the location and condition of the initial disturbance, such that a unique neutral stability curve does not exist. In our problem, it is difficult to relate our results to idealized Görtler theory, as the curvature varies substantially, from zero curvature at the sidewall to high curvature near the corner. Moreover, our base flow is not parallel: the annular geometry means that as the fluid flows radially outward there is considerable fanning out of the flow. As such, standard Görtler theory does not apply directly. What we do find is that there is a small increase in m (from $m = 29$ to 32) with increasing Gr. This corresponds to smaller wavelengths, which is consistent with the velocity boundary layer thickness decreasing with increasing Gr.

It is known[21] that the size and location of the localized heating influences the boundary layer thickness, and therefore it should have an effect on the size (m-value) of the bifurcated structures. The effect, however, is not straight forward to determine. The localized nature is important because if the heater extended all the way to the top endwall, the resulting stratified flow in the bulk tends to inhibit the waviness of the ceiling jet. Being localized, the jet develops up the unheated portion of the inner cylinder, and the subsequent dynamics are dominated by the hydrodynamics rather than the thermodynamics. The heater influences the structures in that the heat flux through it determines the Grashof number, and the jet boundary layer thickness depends on the Grashof number.[21] The other flow regions (away from the ceiling wave) are essentially indistinguishable from those in the corresponding axisymmetric state. For the range of Gr considered, there is very little mean flow modification by the instability and that small amount is localized at the ceiling wave.

The non-axisymmetric solution is a steady state, which we name M29. The instability to three-dimensional flow is via a pitchfork-of-revolution bifurcation breaking the $O(2)$ symmetry. Breaking $O(2)$ symmetry can result in either standing or rotating waves if the bifurcating eigenvalue is complex (symmetry-breaking Hopf bifurcation), and which occurs is very much problem dependent.[27] For our problem however, with the Prandtl number $\sigma = 1$, we have a real eigenvalue that becomes positive, leading to a steady state with broken invariance to rotations but retaining invariance to reflections about a discrete set of meridional planes, so that it retains the parity symmetry. The discrete symmetry group of the solution with m symmetry planes is called D_m, the m-dihedral group. The orientation of these planes is arbitrary, analogous to the axial location of the Taylor cells in the idealized Taylor-Couette problem with an infinitely long annulus. That problem is $O(2)$ symmetric in the axial direction and the first bifurcation is also with a real eigenvalue becoming positive corresponding to a pitchfork-of-revolution bifurcation. Thermal Marangoni convection in an annulus has a geometry more closely related to the present problem, and there too the primary instability is due to a pitchfork-of-revolution bifurcation and results in a steady pattern with a large azimuthal wavenumber that preserves parity. Subsequent bifurcations break parity and lead to rotating waves.[28, 29]

Increasing Gr, and using the M29 solution as an initial condition, the flow either evolves to the M29 state at the higher Gr if the increase in Gr is not too big, or if it is big, the flow may evolve to a different state. Figure 4 shows the time series of the temperature at a point in the middle of the annulus, at $(r, \theta, z) = ((r_o + r_i)/2, 0, 0)$, and the axisymmetric modal kinetic energy, E_0, which is a global measure of the state, for a simulation at $Gr = 7 \times 10^9$ that was initiated with the M29 state at $Gr = 6 \times 10^9$. There is an abrupt adjustment to the sudden increase in heat flux through the heater, followed by a smooth decay of transients over about 5% of the viscous/thermal time, after which the flow has settled onto the steady M29 state at the new Gr value. We have continued the M29 branch
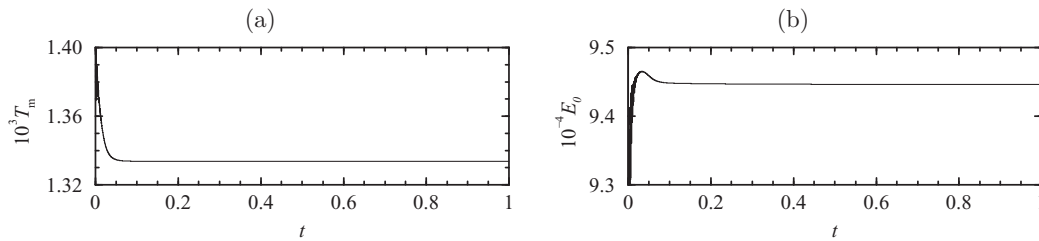
FIG. 4. Time series of (a) T_m, the temperature in the middle of the annular gap $(r, \theta, z) = ((r_o + r_i)/2, 0, 0)$, and (b) E_0 for $Gr = 7 \times 10^9$, starting from the M29 state at $Gr = 6 \times 10^9$ as the initial condition.

up to $Gr = 1.5 \times 10^{10}$. Using different sized jumps in Gr we have also evolved to different branches of solutions, distinguished primarily by their azimuthal wavenumber.

As is typical of problems losing stability to high azimuthal wavenumbers, there is usually a range of stable nonlinear states with comparable wavenumbers known as an Eckhaus band,[30] and the nonlinear selection can play out over a very long time.[31,32] For Gr slightly larger than Gr_{crit}, several additional bifurcations from the now unstable basic state take place, with m close to $m_{crit} = 29$. These additional bifurcated states become stable in secondary bifurcations, also for Gr close to Gr_{crit}, resulting in a number of stable states differing in their corresponding m. All of the steady solutions on the various branches look the same as the M29 solution described in Fig. 3, only differing in their azimuthal wavenumbers. We have found three such branches. The first is the M29 state, the other two, M30 and M32, have azimuthal wavenumbers $m = 30$ and $m = 32$, respectively. Their co-existence extends over considerable ranges in Gr; in Fig. 2(b) we have plotted their modal kinetic energies using various symbols for the solutions we have computed. These solution branches can very likely be continued somewhat further to higher and/or lower Gr using very small increments in Gr, but the computational cost is too large to pursue this further. Which state is selected depends on the initial conditions used. Figure 5 gives a schematic of the Eckhaus bifurcation; using direct numerical simulations we only have direct access to the stable states (M29, M30, and M32, as well as the basic state); the A in the schematic is a measure of the bifurcated state and in Fig. 2, which is the quantitative bifurcation diagram, A is the corresponding modal kinetic energies of each solution branch, E_m. The BS first becomes unstable in a pitchfork-of-revolution bifurcation P_{29} to a steady state M29 breaking the rotational symmetry but preserving the reflection symmetry. On increasing Gr, the (now unstable) basic state undergoes a succession of secondary pitchfork-of-revolution bifurcations (P_{30} and P_{32}) resulting in unstable states (M30 and M32). These states become stable after a sequence of subcritical bifurcations (S). From these secondary bifurcations a variety of unstable mixed modes (MM$_i$) emerge, that may eventually become stable by analogous mechanisms. There are several bifurcations occurring in a narrow range of Gr, and many (both stable and unstable) coexisting states. Similar dynamics associated with Eckhaus instability has been found in rotating convection.[32,33] Further increases in Gr result in interactions between these stable and unstable solutions, typically via homoclinic and heteroclinic collisions, leading to very complex spatio-temporal behavior.
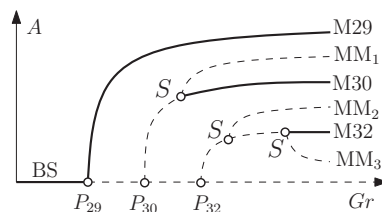

FIG. 5. Schematic of the Eckhaus bifurcation diagram, corresponding to Fig. 2(b) for $Gr < 2 \times 10^{10}$. Solid thick curves correspond to stable states, and dashed curves to unstable ones. Symbols ($\circ$) correspond to bifurcation points: P are pitchforks of revolution where the pure modes (M29, M30, M32...) are born, and S correspond to secondary bifurcations to mixed modes MM$_i$. A is a measure of the non-axisymmetric amplitude of the solution.

B. Three-dimensional periodic solution

Figure 6 show contours of $T - T_0$ for 2 co-existing solutions, M32 and M32s, at $Gr = 2 \times 10^{10}$. Both solutions have azimuthal wavenumber $m = 32$, and are distinguished by a small defect in the M32s state that is located at about $5°$ from the horizontal (almost 3 o'clock, most visible near the outer cylinder, indicated by a $*$). The difference in the modal energy E_{32} for these two states plotted in Fig. 2(b) is a quantitative measure of the effect of this defect. For the M32 state, the kinetic energy is in the underlying axisymmetric flow $m = 0$, and in $m = 32$ and its harmonics. It is a nonlinear, $2\pi/32$-periodic-in-θ, stationary state. In contrast, for the M32s case, the energies are also mostly in these same wavenumbers (with smaller energies), but there is significant energy in a wide band about these. This is due to the presence of the defect in M32s that results in the azimuthal width of the 32 pairs of cells not being uniform (i.e., locally, the cells have a wavelength that is broadly distributed about $2\pi/32$). This defect solution M32s is a steady solution up to $Gr \lesssim 2.5 \times 10^{10}$, and it is a mixed mode like the ones described in the schematic Fig. 5, that has become stable at about $Gr \approx 1.5 \times 10^{10}$. This steady mixed mode is still reflection symmetric, with a single symmetry plane located at the defect, but has broken the discrete rotation symmetry of the pure M32 solution. The symmetry group has shrunk from D_{32} to D_1 (also termed Z_2). The s in the name M32s signifies that this state possesses this spatial reflection symmetry.

The M32s steady solution bifurcates to a periodic solution at about $Gr \approx 2.45 \times 10^{10}$. The defect in M32s leads to a breaking of the discrete reflection symmetry Z_2 and this generically leads to very slow dynamics. The M32s periodic solution at $Gr = 2.5 \times 10^{10}$ has a significantly stronger defect than the steady mixed mode M32s at $Gr = 2 \times 10^{10}$, as is evident from the contours of $T - T_0$ at the top endwall shown in Fig. 7; the defect is at about 8 o'clock and indicated by a $*$. The accompanying movie available online shows a slow drift corresponding to a periodic change in the local azimuthal wavenumber of the vortex pairs or cells. There are still 32 pairs of cells, but their spacing is not uniform, the spacing expands and contracts locally. The local expansion travels clockwise until it reaches the defect and then it travels counter-clockwise and so on, giving a symmetric "sloshing" type of oscillation in the local wavelength. This is clearly seen in the online movie associated with Fig. 7 (multimedia view). In fact, although the solution at any instant in time has broken the invariance to reflections about the meridional plane of the defect, it retains a spatio-temporal symmetry consisting of a half period advance in time together with a reflection through the meridional plane of the defect and changing the sign of the azimuthal velocity, a so-called half-period-flip symmetry. The symmetry group has changed from a purely spatial Z_2 group to a spatio-temporal Z_2 group.

Figure 8 shows a space-time diagram for the M32s state shown in Fig. 7, using θ-profiles of $T - T_0$ at the top endwall at 0.95 of the gap radius. We have extended θ beyond 2π to better illustrate the
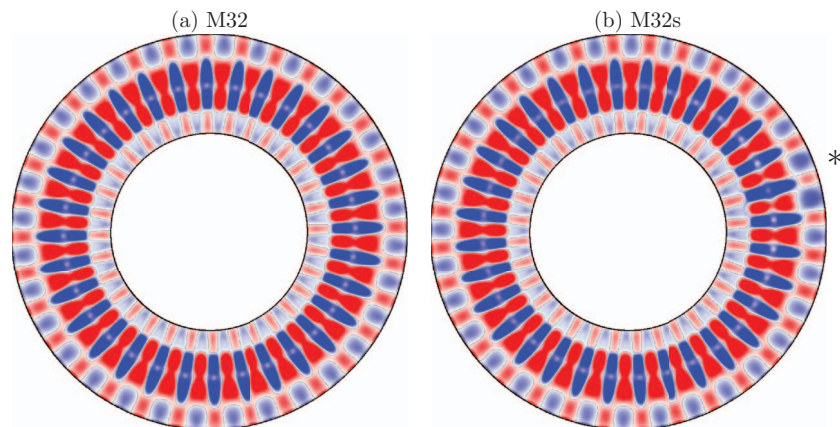

FIG. 6. (a) and (b) Contours of $T - T_0$ (levels between $\pm 5 \times 10^{-6}$), at the top endwall, of two co-existing stable steady states at $Gr = 2 \times 10^{10}$. The $*$ indicates the defect position.
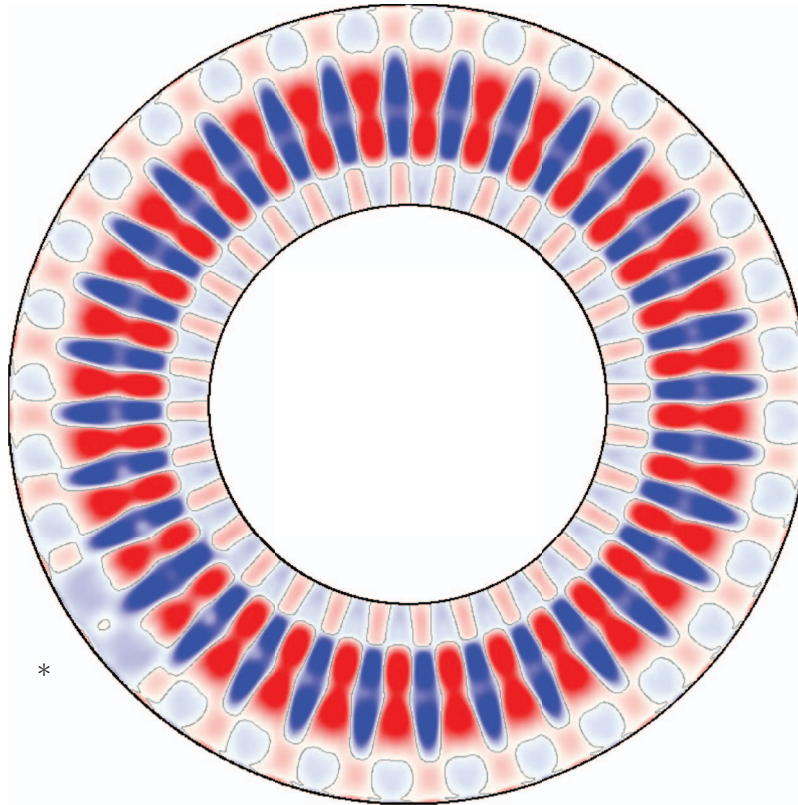
FIG. 7. Contours of $T - T_0$ (at levels between $\pm 10^{-5}$) at the top endwall ($+z$-direction is into the page) of the periodic M32s at $Gr = 2.5 \times 10^{10}$ at $t = 0.64$. The $*$ indicates the defect position. See the online movie for an animation. (Multimedia view) [URL: http://dx.doi.org/10.1063/1.4881435.1]
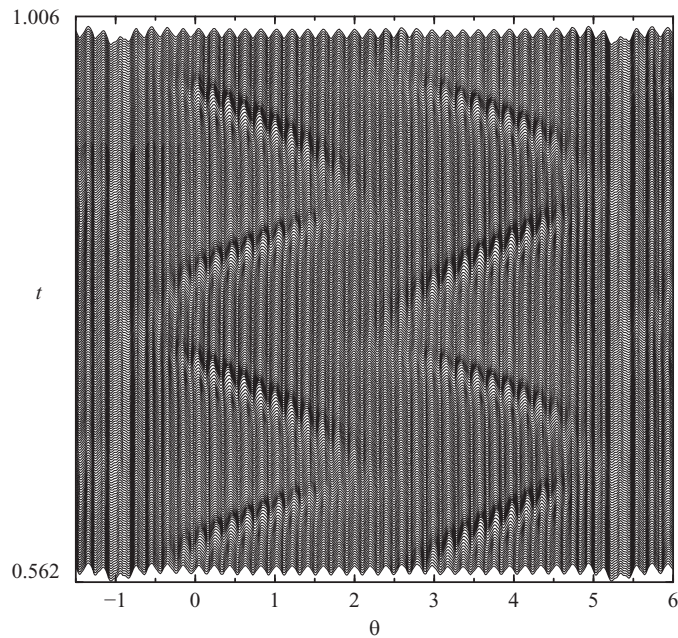

FIG. 8. Profiles of $T - T_0$ at the top endwall at 0.95 of the gap radius for $\theta \in [-1.5, 6]$ over about two periods, $t \in [0.562, 1.006]$ of M32s at $Gr = 2.5 \times 10^{10}$.

space-time dynamics of the solution, which only has a single defect at $\theta = 5.3$, so that the periodic extension repeats the defect at $\theta = 5.3 - 2\pi \approx -1$. The figure shows three distinct features of the problem. They are the underlining $m = 32$ stationary azimuthal periodicity, which is perturbed by an essentially stationary defect, and an $m = 2$ localized perturbation traveling azimuthally as shown in the movie associated with Fig. 7. The travel frequency is 27.96 rad per viscous time. The half-period-flip symmetry described above is evident in this figure, and is due to the localized $m = 2$ wave reflecting off the defect. Note that the parity of the cells where the $m = 2$ wave is located changes depending on the azimuthal direction of travel. Furthermore, the parity associated with the defect changes when the wave reflects off of it. Similar dynamics have been observed experimentally in a Taylor-Couette system where the endwall Ekman vortices play the role of the stationary defect in our problem, and a solitary wave (analogous to our $m = 2$ localized perturbation) bounces back and forth between the endwalls.[34]

C. Three-dimensional quasi-periodic solutions

For $Gr \geq 2.75 \times 10^{10}$, we have found another solution branch which has a dominant azimuthal wavenumber $m = 32$, but in contrast to all the other solution branches described so far, the parity symmetry has been broken globally. We call this asymmetric solution branch M32a. Figure 9 shows contours of $T - T_0$ at the top endwall for M32a at $Gr = 4 \times 10^{10}$. Not only is the spatial aspect of this branch more complicated than that of the other branches, but it is also more complicated temporally. The online movie associated with Fig. 9 illustrates this spatio-temporal complexity, but it is still difficult to succinctly describe its characteristics (multimedia view).
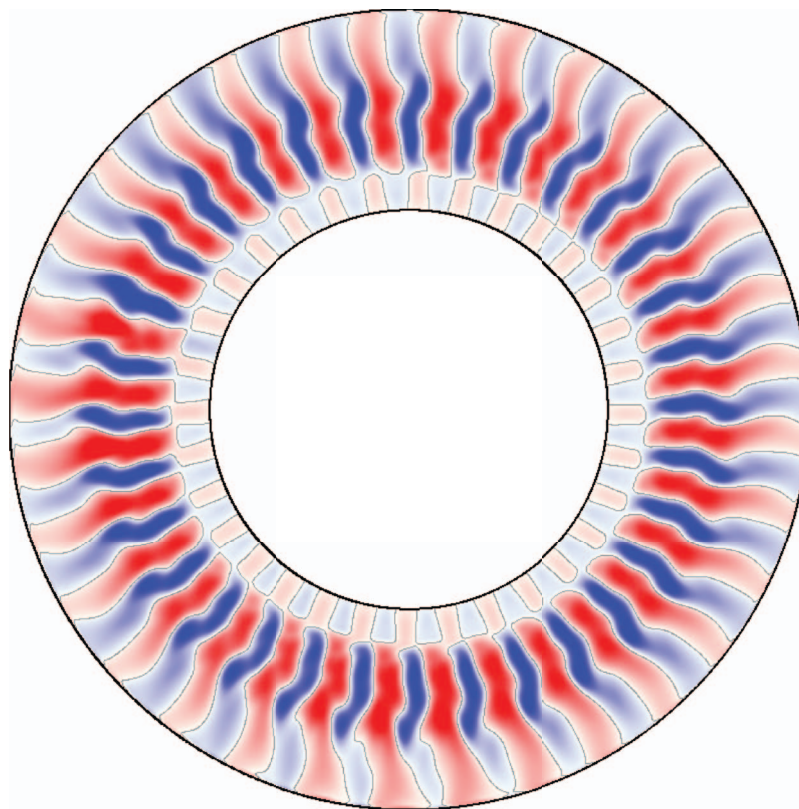

FIG. 9. Contours of $T - T_0$ (levels between $\pm 2 \times 10^{-5}$) at the top endwall ($+z$-direction is into the page) of M32a at $Gr = 4 \times 10^{10}$ at $t = 0.40$. See the online movie for an animation. (Multimedia view) [URL: http://dx.doi.org/10.1063/1.4881435.2]
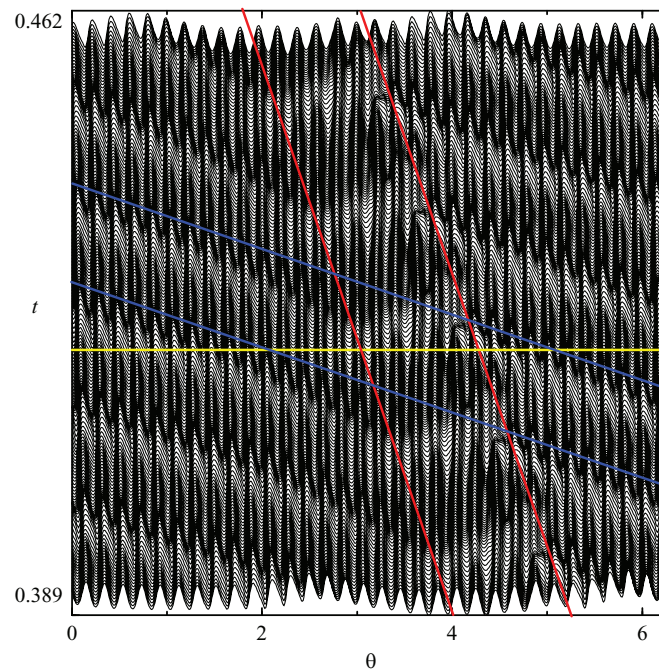
FIG. 10. Profiles of $T - T_0$ at the top endwall at 0.95 of the gap radius for $\theta \in [0, 2\pi]$ over $t \in [0.389, 0.462]$ of M32s at $Gr = 4 \times 10^{10}$. The red lines are the defect boundary, and the blue lines are an $m = 2$ localized perturbation. The yellow line is a t-constant section.

The analysis of the dynamics is more complicated than in the M32s limit cycle case, even with the use of the animations. However, it still remains a quasi-one-dimensional pattern in the azimuthal direction, and the corresponding space-time diagram, shown in Fig. 10 provides considerable insight. There are two distinct wave patterns evident. One is due to the defect, which is barely visible in the snapshot of Fig. 9. The defect is much broader than in the M32s case, bounded by the red lines in Fig. 10, and in this case the defect is not stationary, but has a very slow azimuthal drift, with an averaged frequency of 28.12 rad per viscous time (about 4.5 circuits per viscous time). The underlying $m = 32$ pattern also drifts azimuthally with the defect as a whole. The second wave pattern, as in the M32s case, is due to an $m = 2$ localized perturbation traveling azimuthally, indicated by the blue lines in Fig. 10, with a traveling frequency of 237.5 rad per viscous time. At any time (see the horizontal yellow line in Fig. 10), we observe two localized perturbations intersecting the yellow line, so it is an $m = 2$ perturbation. This localized perturbation is more intense and faster than in the M32s solution at $Gr = 2.5 \times 10^{10}$, and instead of reflecting at the defect it passes through it. The defect cannot stop the localized perturbation, and in fact when the $m = 2$ perturbation interacts with the defect, it drags it azimuthally a small amount. The two associated rotation frequencies are incommensurate, and so M32a is quasi-periodic. Since the parity (reflection) symmetry of M32a is broken, applying the K symmetry operation (Eq. (5)) results in the conjugate state with modulated rotations of the opposite sense. There are two symmetrically related M32a states, one left-handed and the other right-handed.

Figure 11 shows a snapshot of three-dimensional isosurfaces of $\eta - \eta_0$; see the online movie for an animation (multimedia view) which clearly shows the dynamics we have extracted from the space-time diagram in Fig. 10. The fast moving $m = 2$ localized perturbation is clearly appreciated. Moreover, the whole pattern shows a pulsation associated with the collision of the $m = 2$ perturbation with the defect, dragging it azimuthally and resulting in a ratcheting motion. The defect location is still very difficult to distinguish in the movie, while the ratcheting motion is difficult to appreciate in the space-time diagram. It is the combined use of both visualization tools that makes it possible to provide a precise description of the dynamics.
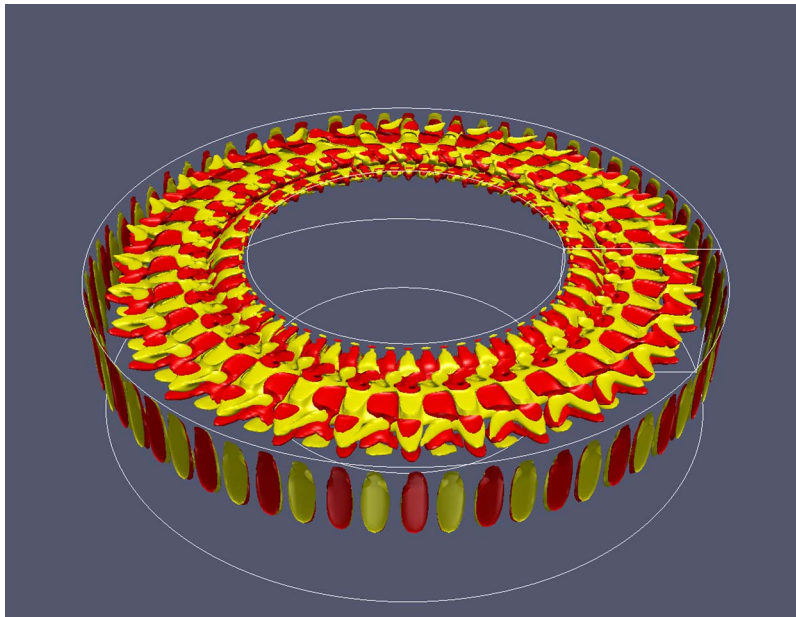
FIG. 11. Snapshot of isosurfaces of $\eta - \eta_0$ at levels ± 2000 for M32a at $Gr = 4 \times 10^{10}$. See the online movie for an animation. (Multimedia view) [URL: http://dx.doi.org/10.1063/1.4881435.3]

Figure 12 shows how the mean E_2, which is a proxy measure of the strength of the solitary $m = 2$ wave, and the period τ of the solitary wave in M32s and M32a varies with Gr. What is evident is that E_2 grows rapidly from very small values with increasing Gr and that $E_2 \sim O(1)$ corresponds to the switch from M32s to M32a. In some sense, the solitary wave in M32s de-pins from the defect as it becomes stronger with increasing Gr. The pinned state M32s has period $\tau \to \infty$ for decreasing Gr, suggesting that it is born in a SNIC (saddle-node-on-an-invariant-circle) bifurcation when the steady M32s solution becomes time-dependent. When E_2 is small, the solitary wave bounces back and forth off of the defect, and when it is strong enough ($E_2 > 1$) it is able to push through the defect and we have state M32a. The behavior of τ is typical of de-pinning scenarios, which are never simple,[35] but the M32a branch has the general behavior of the period becoming unbounded as the pinning region is approached, the region near the pinning is populated with multiple states with complex dynamics, and the period reduces and relaxes to a more uniform oscillation as the pinning region is departed. As Gr is increased beyond 4×10^{10}, the quasi-periodic nature of M32a is lost as
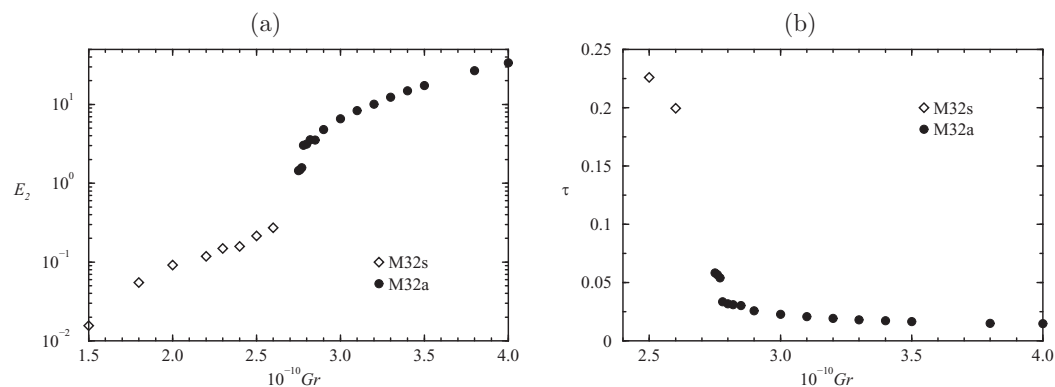

FIG. 12. Variations with Gr of (a) mean modal kinetic energies in azimuthal wavenumber $m = 2$ and (b) periods, of the M32s and M32a states.

individual cells become strongly distorted locally. Dynamically, this corresponds to a torus breakup event, whose detailed analysis we postpone to a later date.

V. DISCUSSION

The connection between the M32s and M32a branches of solutions is not obvious. M32s is a symmetric limit-cycle and M32a are two conjugate asymmetric quasi-periodic states. We have spent a considerable amount of time and computational resources trying to close the gap between the M32s and M32a families. We have done that by continuation: starting with a solution on one branch and increasing or decreasing Gr by a very small amount, producing the curves corresponding to the families M32s and M32a. However, it has been impossible to close the gap: when we move into the gap, the solutions exhibit very long transients and finally evolve into the steady pure mode M32 family. Furthermore, very close to the end of the branches, it looks like there is a multiplicity of solutions within the same family. In particular, for the M32a branch as shown in Fig. 12, there are different solutions differing in the frequencies associated with the defect motion. We have seen in both laboratory experiments and associated numerical simulations of Taylor-Couette flow[36–38] that the small parameter region between a symmetric limit cycle and asymmetric quasi-periodic states is populated by a complicated bifurcational process. Analogous dynamics also seem to be at play in the present problem.

The behavior described above, consisting of different solution branches that are not connected by a single bifurcation, but instead there is a gap between them with complex dynamics and multiplicity of solutions, has been observed in a variety of different fluid dynamics problems, both numerically and experimentally. These dynamics are usually related to symmetry breaking, as in the present problem. One example in Taylor-Couette flow has been extensively studied,[36–38] where the small parameter gap between a symmetric limit cycle and asymmetric quasi-periodic states is populated by a complicated bifurcational process involving homoclinic cascades. Another example is in rotating convection or in small aspect ratio Taylor-Couette flow,[39] where the breaking of the $SO(2)$ rotational symmetry results in a small parameter gap (a pinning region) that separates rotating wave solutions precessing in opposite directions. On approaching this pinning region close to the Hopf bifurcation results in very complex homoclinic and heteroclinic dynamics.

This type of complex behavior has also been observed in low-dimensional models, using normal forms. Knobloch and co-workers[40,41] have analyzed the influence of imperfections in a bifurcation breaking the rotational symmetry while preserving the reflection symmetry in $O(2)$-equivariant problems. This is what happens in our pitchfork-of-revolution bifurcation, with the imperfection corresponding to the formation of the steady defect that we observe in the M32s family, completely breaking the $O(2)$ symmetry and replacing the reflection symmetry with a half-period-flip symmetry. The dynamics of secondary bifurcations observed in the low-dimensional model[40,41] is complex, and typically involves sequences of global bifurcations. The possible scenarios were described in detail and the results were related to the dynamics associated with parity-breaking instabilities of spatially periodic patterns. In particular, they found two families of stable solutions (SW and TW, analogous to our steady and traveling defect in M32s and M32a), whose space-time diagrams (Fig. 2 of Ref. 41) are very similar to the space-time diagrams of our M32s and M32a families. They also found that the connection between both families involves a complex bifurcation scenario in a narrow parameter range that includes homoclinic connections, and therefore very slow dynamics.

Our case is difficult to analyze using very low-dimensional models because of the existence of the Eckhaus band and the associated dynamics. This dynamics was described theoretically in a finite system using the Ginzburg-Landau equation,[30] and is illustrated schematically in Fig. 5. On increasing Gr the BS becomes unstable and undergoes a succession of pitchfork-of-revolution bifurcations resulting in unstable states that become stable after a sequence of subcritical bifurcations (S). From these secondary bifurcations, a variety of unstable mixed modes (termed MM_i in the figure) emerge. Further increases in Gr results in interactions between these stable and unstable solutions, typically via homoclinic and heteroclinic collisions, resulting in very complex spatio-temporal behavior including chaotic attractors/repellors. The analysis using the Ginzburg-Landau equation[30]

describes only the formation of the coexisting stable pure modes and the unstable mixed modes. The detailed normal form analysis[40,41] describes the dynamics of two particular families of solutions with defects (equivalent to our M32s and M32a branches), but it is unable to connect these families with the other coexisting stable and unstable states originating in the Eckhaus bifurcational process. A combined approach using both techniques is very challenging, and has not been attempted yet to our knowledge.

We conclude by mentioning that solitary waves closely resembling our M32s family have been observed experimentally[34] in a finite Taylor-Couette system, where the endwall Ekman vortices of the finite apparatus play the role of the imperfections breaking the $O(2)$ symmetry that corresponds to the idealized infinite cylinders problem. This experimental system does not have the M32a family and their complex interaction with M32s. The "defects" in this laboratory system are the endwalls in the finite Taylor-Couette apparatus, and these do not move, therefore states analogous to the M32a family, with moving defects, are not physically achievable. We should note that the solitary waves that were observed in the experiments sometimes were transitory, lasting about 100 viscous time units, but some were also observed to persist for over 1000 viscous time units, corresponding to several hours in the physical experiment. It is possible that some of the solutions in our M32s and M32a families are also transients, as in this experiment, and as we reported earlier, for $2.6 \times 10^{10} < Gr < 2.75 \times 10^{10}$, the solitary waves are transitory and the flow eventually evolves to the pure M32 state. However, for smaller and larger Gr we have found both M32s or M32a states with solitary waves persisting for about one viscous time (corresponding to several months of computation) and co-existing pure M32 states, and which is obtained depends on the initial conditions.

VI. CONCLUSIONS

We have analyzed the dynamics of natural convection in an annulus driven by a constant heat-flux finite segment on the inner cylinder. The details of the basic axisymmetric state had been previously studied up to large heat fluxes, $Gr = 10^{10}$, where the flow is dominated by very thin boundary and shear layers.[21] Here, we investigate its stability and transition to three-dimensional spatio-temporal complexity.

We have found that the base state, steady and axisymmetric, is stable at very high Grashof numbers, up to $Gr = Gr_{\text{crit}} \approx 5.9 \times 10^9$. The steady and axisymmetric base state becomes three-dimensional in a pitchfork-of-revolution bifurcation. The bifurcated state is steady and parity symmetric with an $m = 29$ azimuthal wavenumber. On increasing Gr, other steady states with different azimuthal wavenumbers appear in an Eckhaus instability process. We have found some of the stable pure modes (the M30 and M32 solutions) resulting from this process. We have not explored in detail the Eckhaus process as it is already well known, and instead we have focused on additional families of solutions with more complex dynamics stemming from the presence of defects.

We have found periodic solutions (limit cycles) with a space-time parity symmetry, and quasi-periodic solutions with broken parity symmetry. Both branches of solutions include a defect that strongly affects the dynamics. The two branches correspond to the steady (SW) and traveling waves (TW) usually associated with breaking the $O(2)$ symmetry with defects, with the defects resulting from interactions between the pure and mixed modes typical of the Eckhaus bifurcational process. The correspondence is that on the M32s branch the defect location is stationary, and in the two parity-conjugated M32a branches the defect travels either clockwise or anticlockwise. The types of dynamics associated with M32s and M32a are typical of pattern-forming systems with broken $O(2)$ symmetry, and the normal-form analysis of such systems shows that spatial inhomogeneities (such as due to the defect in our example) lead to pattern drifts that can be quite complex, involving cascades of complex bifurcations.[40,41] Further analysis of such models, although very challenging, may provide additional insight into the spatio-temporal dynamics of this problem. We hope that the rich defect dynamics displayed by the system we have analyzed here will stimulate further research in this direction.

ACKNOWLEDGMENTS

[1] A. Bejan, *Convection Heat Transfer*, 2nd ed. (John Wiley & Sons, New York, 1995).

[2] G. K. Batchelor, "Heat transfer by free convection across a closed cavity between vertical boundaries at different temperatures," Q. Appl. Math. **12**, 209 (1954).

[3] J. W. Elder, "Laminar free convection in a vertical slot," J. Fluid Mech. **23**, 77 (1965).

[4] A. E. Gill, "The boundary-layer regime for convection in a rectangular cavity," J. Fluid Mech. **26**, 515 (1966).

[5] B. Podvin and P. Le Quéré, "Nonlinear dynamics between two differentially heated vertical plates in the presence of stratification," Theor. Comput. Fluid Dyn. **27**, 89 (2013).

[6] S. Kimura and A. Bejan, "The boundary-layer natural-convection regime in a rectangular cavity with uniform heat-flux from the side," J. Heat Transfer **106**, 98 (1984).

[7] W. Lin, S. W. Armfield, and J. C. Patterson, "Unsteady natural convection boundary-layer flow of a linearly-stratified fluid with $Pr < 1$ on an evenly heated semi-infinite vertical plate," Int. J. Heat Mass Transfer **51**, 327 (2008).

[8] M. Wang, S. Fu, and G. Zhang, "Large-scale spiral structures in turbulent thermal convection between two vertical plates," Phys. Rev. E **66**, 066306 (2002).

[9] P. Hall, "Vortex-wave interactions: Long-wavelength streaks and spatial localization in natural convection," J. Fluid Mech. **703**, 99 (2012).

[10] Z. Gao, A. Sergent, B. Podvin, S. Xin, P. Le Quéré, and L. S. Tuckerman, "Transition to chaos of natural convection between two infinite differentially heated vertical plates," Phys. Rev. E **88**, 023010 (2013).

[11] G. N. Ivey, "Experiments on transient natural convection in a cavity," J. Fluid Mech. **144**, 389 (1984).

[12] S. G. Schladow, J. C. Patterson, and R. L. Street, "Transient flow in a side-heated cavity at high Rayleigh number: A numerical study," J. Fluid Mech. **200**, 121 (1989).

[13] J. C. Patterson and S. W. Armfield, "Transient features of natural convection in a cavity," J. Fluid Mech. **219**, 469 (1990).

[14] S. W. Armfield and J. C. Patterson, "Direct simulation of wave interactions in unsteady natural convection in a cavity," Int. J. Heat Mass Transfer **34**, 929 (1991).

[15] S. Paolucci and D. R. Chenoweth, "Transition to chaos in a differentially heated vertical cavity," J. Fluid Mech. **201**, 379 (1989).

[16] S. W. Armfield and J. C. Patterson, "Wave properties of natural-convection boundary layers," J. Fluid Mech. **239**, 195 (1992).

[17] F. Xu, J. C. Patterson, and C. Lei, "On the double-layer structure of the boundary layer adjacent to a sidewall of differentially heated cavity," Int. J. Heat Mass Transfer **51**, 3803 (2008).

[18] R. Puragliesi, A. Dehbi, E. Leriche, A. Soldati, and M. O. Deville, "DNS of buoyancy-driven flows and Lagrangian particle tracking in a square cavity at high Rayleigh numbers," Int. J. Heat Fluid Flow **32**, 915 (2011).

[19] G. de Vahl Davis and R. W. Thomas, "Natural convection between concentric vertical cylinders: High speed computing in fluid dynamics," Phys. Fluids **12**(Suppl. II), 198 (1969).

[20] V. Prasad and F. A. Kulacki, "Free convective heat transfer in a liquid-filled vertical annulus," J. Heat Transfer **107**, 596 (1985).

[21] J. M. Lopez, M. Sankar, and Y. Do, "Constant-flux discrete heating in a unit aspect-ratio annulus," Fluid Dyn. Res. **44**, 065507 (2012).

[22] S. Hugues and A. Randriamampianina, "An improved projection scheme applied to pseudospectral methods for the incompressible Navier-Stokes equations," Int. J. Numer. Methods Fluids **28**, 501 (1998).

[23] I. Mercader, O. Batiste, and A. Alonso, "An efficient spectral code for incompressible flows in cylindrical geometries," Comput. Fluids **39**, 215 (2010).

[24] M. Avila, M. Grimes, J. M. Lopez, and F. Marques, "Global endwall effects on centrifugally stable flows," Phys. Fluids **20**, 104104 (2008).

[25] J. M. Floryan, "On the Görtler instability of boundary layers," Prog. Aerospace Sci. **28**, 235 (1991).

[26] W. S. Saric, "Görtler vortices," Annu. Rev. Fluid Mech. **26**, 379 (1994).

[27] E. Knobloch, "Symmetry and instability in rotating hydrodynamic and magnetohydrodynamic flows," Phys. Fluids **8**, 1446 (1996).

[28] S. Hoyas, H. Herrero, and A. M. Mancho, "Thermal convection in a cylindrical annulus heated laterally," J. Phys. A **35**, 4067 (2002).

[29] S. Hoyas, H. Herrero, and A. M. Mancho, "Bifurcation diversity of dynamic thermocapillary liquid layers," Phys. Rev. E **66**, 057301 (2002).

[30] L. S. Tuckerman and D. Barkley, "Bifurcation analysis of the Eckhaus instability," Physica D **46**, 57 (1990).

[31] Y. Liu and R. E. Ecke, "Eckhaus-Benjamin-Feir instability in rotating convection," Phys. Rev. Lett. **78**, 4391 (1997).

[32] J. M. Lopez, F. Marques, I. Mercader, and O. Batiste, "Onset of convection in a moderate aspect-ratio rotating cylinder: Eckhaus-Benjamin-Feir instability," J. Fluid Mech. **590**, 187 (2007).

[33] F. Marques and J. M. Lopez, "Influence of wall modes on the onset of bulk convection in a rotating cylinder," Phys. Fluids **20**, 024109 (2008).

[34] R. J. Wiener and D. F. McAlister, "Parity breaking and solitary waves in axisymmetric Taylor vortex flow," Phys. Rev. Lett. **69**, 2915 (1992).

[35] F. Marques, A. Meseguer, J. M. Lopez, J. R. Pacheco, and J. M. Lopez, "Bifurcations with imperfect SO(2) symmetry and pinning of rotating waves," Proc. R. Soc. London, Ser. A **469**, 20120348 (2013).

[36] J. Abshagen, J. M. Lopez, F. Marques, and G. Pfister, "Symmetry breaking via global bifurcations of modulated rotating waves in hydrodynamics," Phys. Rev. Lett. **94**, 074101 (2005).

[37] J. Abshagen, J. M. Lopez, F. Marques, and G. Pfister, "Mode competition of rotating waves in reflection-symmetric Taylor-Couette flow," J. Fluid Mech. **540**, 269 (2005).

[38] J. Abshagen, J. M. Lopez, F. Marques, and G. Pfister, "Bursting dynamics due to a homoclinic cascade in Taylor–Couette flow," J. Fluid Mech. **613**, 357 (2008).

[39] J. R. Pacheco, J. M. Lopez, and F. Marques, "Pinning of rotating waves to defects in finite Taylor-Couette flow," J. Fluid Mech. **666**, 254 (2011).

[40] E. Knobloch, J. Hettel, and G. Dangelmayr, "Parity breaking bifurcation in inhomogeneous systems," Phys. Rev. Lett. **74**, 4839 (1995).

[41] G. Dangelmayr, J. Hettel, and E. Knobloch, "Parity-breaking bifurcation in inhomogeneous systems," Nonlinearity **10**, 1093 (1997).